Chapter 13

Single and Two-Phase Heat Transfer Enhancement Using Longitudinal Vortex Generator in Narrow Rectangular Channel

Yan-Ping Huang, Jun Huang, Jian Ma, Yan-Lin Wang,
Jun-Feng Wang and Qiu-Wang Wang

Additional information is available at the end of the chapter

http://dx.doi.org/10.5772/53713

1. Introduction

In the past several decades, heat transfer enhancement techniques have rapidly developed and have been widely employed in many industrial fields. Up to now, these techniques have entered a stage of the so-called third generation, in which the use of longitudinal vortex generator is one of representative methods. When fluid flows over a barrier, different kinds of vortices will come into being. Among these vortices, longitudinal vortex (LV) has a swirling axis parallel to the main flow direction and moves downstream swirly around this axis and exhibits strong three-dimensional characteristics. Such a barrier is technically defined as longitudinal vortex generator (LVG). From the heat transfer perspective, the three-dimensional swirling movement of LV is useful for heat transfer enhancement (Sohankar, A. & Davidson, L. 2001), and can be employed in many industrial fields such as high temperature vane cooling, convective heat transfer in narrow channels, fin tube heat transfer enhancement, and etc. Therefore, the heat transfer enhancement of LV has been paid close attention and a large number of relevant references can be found, especially in the gas heat transfer cases (Schubauer, G.B. & Spangenberg, 1960; Johnson T.R. & Joubert P.N., 1969).

However, very few researchers chose water as working medium in their studies on heat transfer enhancement by LV in narrow rectangular channels (Chen, Q.Y., et al., 2006; Islam, M.S., et al., 1998; Sohankar, A. & Davidson, L., 2001; Wang, Q.W., et al., 2007). In fact, water is the most important working fluid and widely used in power industry field. For example in some plate-fin water-water heat exchangers, water flows through a series of narrow rectangular channels to release or absorb heat from the other side. If LVG is chosen to increase the heat transfer capability and enhance superficial heat transfer efficiency for such

type of heat exchanger, the single and two-phase heat transfer coefficient must be available during design process. In the case of the rod-type fuel assembly used in a pressurized-water nuclear reactor, the vanes on spacers play a role similar to LVG, which reconstructs the velocity and temperature fields and enhances the heat transfer. In this case, the improvement of Critical Heat Flux (CHF) of fuel assembly must also be taken into account (Crecy F., 1994).

For the above mentioned reasons and experiences, the single and two-phase flow and heat transfer and CHF in a narrow rectangular channel with LVG have been studied in this chapter.

2. CFD method and theoretical basis for LVG design

In this study, the LVG was composed of four pairs of rectangular ribs. To optimize the LVG's configuration, the dimensions of a single rib and the whole layout of all ribs were elaborately designed with the help of computational fluid dynamics (CFD) simulation. In the simulation, the computation domain was a narrow rectangular channel which had an aspect ratio of 13 (the channel width to narrow gap ratio), a narrow gap of 3.0mm, and a length to hydraulic diameter ratio of 80.0. And, four pairs of ribs were periodically installed on the unilateral wall in the narrow rectangular channel. In our previous work (Wang L. & Wang Q.W., 2005), each single rectangular rib (with a 50°attack angle, 1.2mm in height, 2.0mm in width, 10.0mm in length, 10.0mm in transverse distance, 100.0mm in axial distanc) had the same original parameters.

CFX5-Build was used as a geometry and mesh generation pre-processor module. Fig.1 shows the computation domain including adjacent two pairs of LVGs and the mesh that were constructed for the simulation using CFX-5 computer code. Mesh generation was based on multi-block structured hexahedral grid. Number of the independent elements in the simulated mesh are 232,632. The surface mesh was created using a Delaunay method and the volume mesh was created through advancing front and inflation method. The mesh elements on the wall surfaces were refined to improve the accuracy in these regions.

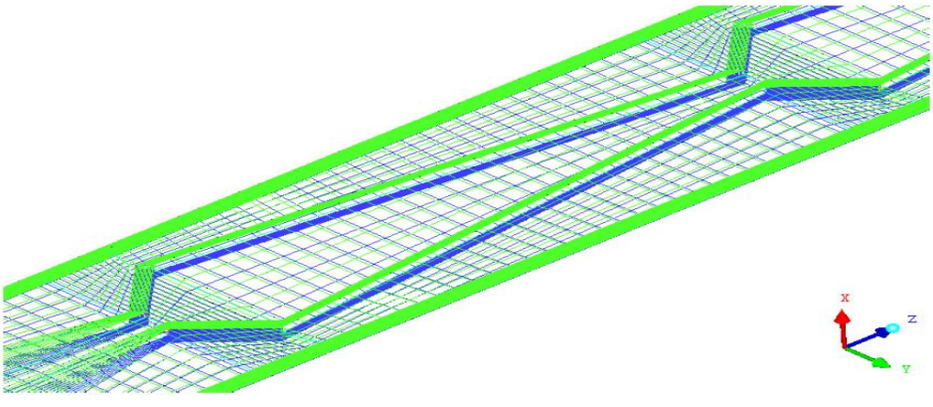

Figure 1. Mesh distribution in the computation domain.

To overcome the decoupling of pressure and velocity, a single cell, unstaggered, collocated grid was used. The continuity equation was a second order central difference approximation to the first order derivative in velocity, modified by a fourth derivative in pressure which

acts to redistribute the influence of the pressure. This overcame the problem of checker board oscillations. Transient term took the second order backward Euler scheme, which is robust, implicit, conservative in time, and does not create a time step limitation. Following the standard finite element approach, shape functions were used to evaluate the derivatives for all the diffusion terms. Pressure gradient term was evaluated using the shape functions. Advection term took high Resolution Scheme which does not violate boundedness principles.

The boundary normal velocity was specified at the inlet. The Reynolds numbers based on the channel hydraulic diameter varied from 3200 to 31400. No slip boundary condition was applied to the wall surfaces. Only the wall, on which the ribs stands, was provided with constant heat flux while the other wall were heat insulated. The heat flux was initialized to the value of 100 kW/m^2. The average static pressure was specified at the outlet. De-ioned water was chosen as working fluid.

The Shear Stress Transport (SST) model was used for turbulence modeling. Scalable Wall-Functions were used for near wall treatment. In the calculations, the coupled solver was used to solve the governing equations. During the simulation process, only a single parameter varied while the other parameters kept constant. In each case, friction factor and Nusselt number were calculated as below and they were used for evaluating flow drag and convective heat transfer in the channel.

$$f = \frac{8\tau_{\mathrm{w}}}{\rho u^2} \tag{1}$$

$$Nu = \frac{q_{\mathrm{w}} D_{\mathrm{h}}}{\lambda (T_{\mathrm{w}} - T_{\mathrm{f}})} \tag{2}$$

The weighted factor for every parameter could be calculated as bellow:

$$\varphi_{Nu} = \left| \left(Nu_{\mathrm{av}} - Nu_{\mathrm{min}} \right) / \Delta x \right| \tag{3}$$

$$\varphi_{f} = \left| \left(f_{\mathrm{av}} - f_{\mathrm{min}} \right) / \Delta x \right| \tag{4}$$

where Δx represents every normalized parameter as $\beta/180°$, X/L, h/H, $b/(B/2)$, s/B and $a/(B/2)$.

The computation result at Reynolds number of 30000 and Prandtl number of 3.7 was shown in Fig.2, but it was difficult to directly determine which parameter has the most marked effect on Nusselt numbers and friction factors. Therefore, it should need a compromise between flow drag and convective heat transfer to optimize the LVG's configuration. The orthogonal method for multi-parameters optimization was proposed by Taguchi and was used for the current case. By choosing dimensionless *JF* number proposed by Yun (Yun J. Y., & Lee K. S., 2000) as target function, the general performance evaluation criteria of heat transfer enhancement with LVG could be expressed as:

$$JF = \left(j_{\mathrm{LVG}} / j_{\mathrm{S}} \right) / \left(f_{\mathrm{LVG}} / f_{\mathrm{S}} \right)^{1/3} \tag{5}$$

where $j = Nu / (Re \cdot Pr^{1/3})$.

By calculation and comparison based on Eq. (5), the final optimized LVG's configuration was obtained as shown in Fig.3. Each single rib had an uniform dimension of 14.0mm×2.2mm×1.8mm, each pair of ribs had an uniform attack angle of 44° and an uniform transverse distance of 4mm, and the total four pairs of ribs had an uniform axial distances of 100.0mm.

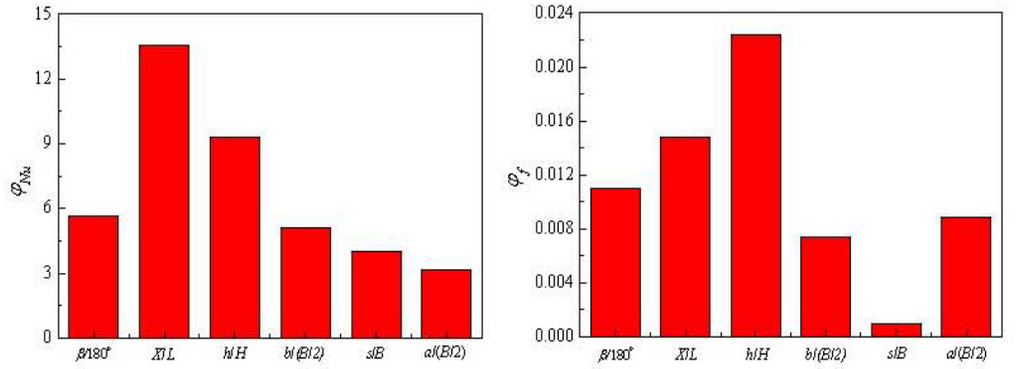

Figure 2. Weighted Nusselt number and friction factor of different parameters.

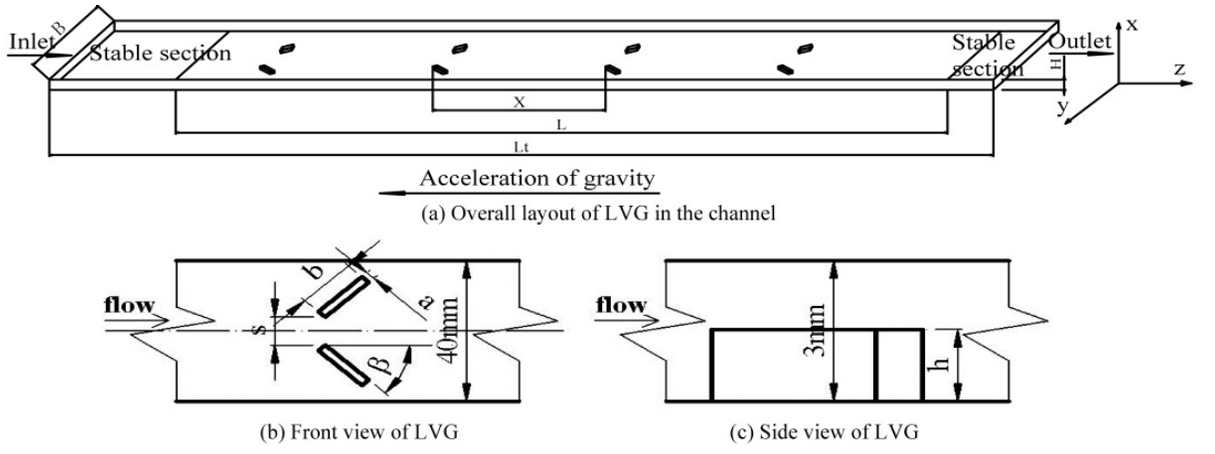

Figure 3. Schematic of the final LVG configuration.

3. Experimental system and method

The experiments were conducted at the flow and heat transfer experimental platform in CNNC Key Laboratory on Nuclear Reactor Thermal Hydraulics Technology, Nuclear Power Institute of China. The experimental apparatus mainly consisted of experimental loop, test section, instruments, power supplier, and data acquisition system. Each part was described in details as following.

1. Experimental loop

It was shown in Fig.4 that the experimental loop contains pumps, pre-heater, pressurizer, flow-meters, test section, mixer, heat exchanger and some valves. Among these parts, the

piston pump supplied the loop with de-ioned water from the water tank, the pressurizer kept system pressure steady, the circulating pump drived de-ioned water flow in the loop, the mixer mixed hot water from the outlet of the test section with cold water from the cyclic pump, the flow-meters were used for measuring flow rates in the cyclic pump and test channel, and the heat exchanger cooled water from the outlet of the mixer.

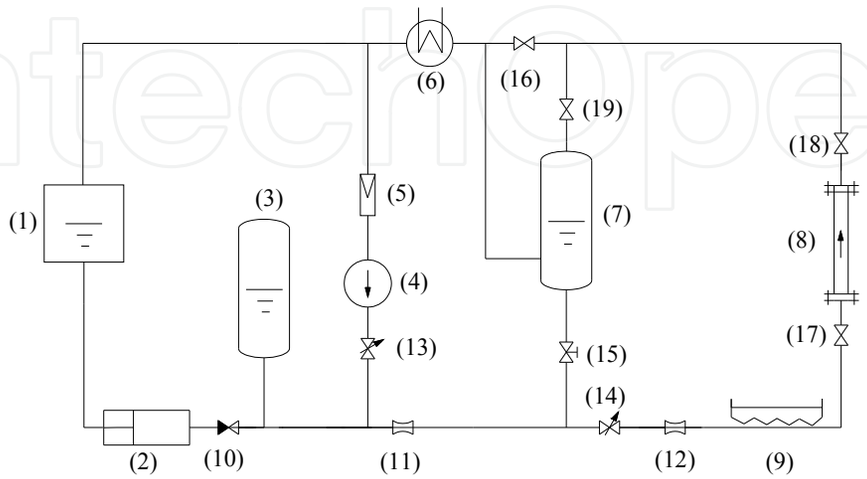

(1) water tank (2) piston pump (3) pressurizer (4) circulating pump (5) filter (6) heat exchanger (7) mixer (8) test section (9) preheater (10) check valve (11),(12) flow-meter (13),(14) flow regulator (15),(16),(17),(18) automatic control valve (19) manual valve

Figure 4. Flow chart of the experimental Loop.

2. Test section

The test section was designed for the two different kinds of experiments, viz., flow and heat transfer experiment and visualization experiment, and mainly consisted of two holders, quartz glass and heating plate. Both the holders and the heating plate were made of 0Cr18Ni10Ti stainless steel, and the other accessories material was chosen dependent on their functions. The total four pairs of rectangular ribs as LVG were machined on the heating plate surface according to the final LVG configuration shown in Fig.3. The whole structure of the test section was shown in Fig.5.

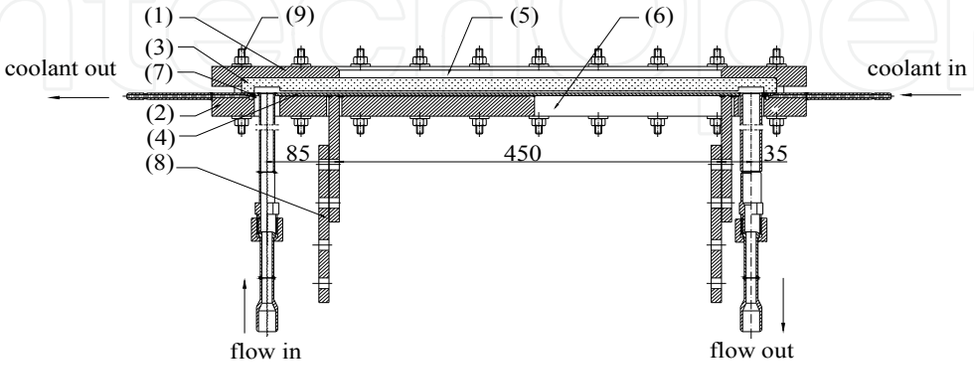

(1) upper holder (2) lower holder (3) quartz glass (4) heating plate (5) window for visual velocity measuring (6) empty space for infrared thermo-image recording temperature (7) "O" type ring (8) copper plate (9) bolts, nuts, and washers

Figure 5. Schematic of the test Section.

There was a narrow rectangular groove with the dimension of 600mm×40mm×3mm on a piece of quartz glass. The heating plate was 610mm×50mm×3mm in dimension. So the close combination between the narrow rectangular groove and the heating plate could form a narrow channel with the cross section of 40mm×3mm in dimension, and the effective heating length was 450mm in dimension as the two ends occupation of the copper plates for power inputs. Thus, the narrow channel had a hydraulic diameter of 5.58mm and a length to diameter ratio of 80.65. The waterproof of the narrow channel was guaranteed by a silicon latex "O" type ring. There was a coolant channel on the surface of the lower holder contacting the outer wall of the heating plate to keep the "O" type ring at an acceptable temperature and prevent from heat concentration on the edges and destruction of heating plate in case of high heat flux. The electrical insulation between the heating plate and the holders was achieved by a piece of isinglass paper with the thickness of 0.3mm. To facilitate recording the outer wall temperature by the use of infrared thermo-imager, a rectangular empty space of 235mm×40mm was machined on the tail half lower holder below the heating plate and located in the region of downstream two pairs of LVG. The cross sectional details of the test section with the empty space were shown in Fig.6.

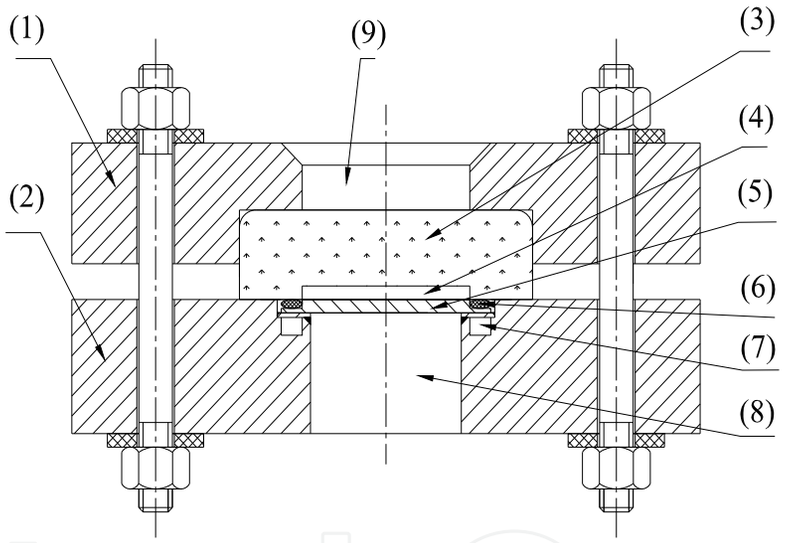

(1) upper holder (2) lower holder (3) quartz glass (4) narrow rectangular channel (5) heating plate (6) "O" type ring (7) cooling channel (8) empty space for thermal infrared imager recording temperature (9) window for visual velocity measuring

Figure 6. Schematic of the cross section of the test section with an empty space.

To accurately measure the outer wall temperatures, the total 45 orifices were drilled in 6 rows and in 15 columns respectively in the span-wise and stream-wise directions on the lower holder for the access of 45 thermocouples(24 were located in the region of the empty space) to the outer wall; each orifice was 3mm in diameter, and each span-wise distance was 9mm while each stream-wise distance is 30mm. To measure the pressure drop across the test section, a hole with 13mm in diameter was drilled near the first end copper plate on the lower holder for the access of the first pressure tap to the channel, there was no need to drill another hole downstream 424mm because the second pressure tap crossed the empty space and could be directly connected with the hole on the heating plate.

After the thermocouples being fixed, the two bakelite plates were used for holding the thermocouples, and many layers of asbestos piece as heat insulation stuff filled the empty space between the two bakelite plates. This measure could prevent from heat loss brought by the empty space. Before conducting the flow and heat transfer experiment, the test section was wrapped with a thick layer of asbestos piece for further heat insulation. It was noticed that the empty space on the lower holder need to be exposed to atmosphere so that the camera could easily receive the infrared thermo-images in the visualization experiments.

3. Instruments, power supplier, and data acquisition system

The pressures at the inlet and outlet of the test channel were measured using SMART3000 type pressure transducer. The pressure drop across the test channel was measured using SMART3000 type differential pressure transducers. The pressure transducer and the differential pressure transducers were respectively connected to the fittings attached to the hole with 13mm in diameter on the lower holder and to the other one downstream 424mm on the heating plate. The accuracy in the measurement of the inlet and outlet pressures was about ±3kPa. The accuracy in the measurement of the pressure drop across the test channel was about ±30Pa. The pressure at the inlet of coolant channel was measured using a manometer with an accuracy of ±10kPa.

The flow rates of the test fluid and coolant were respectively measured using a Venturi-tube type flow-meter which coupled with a SMART3000 type differential pressure transducer with an accuracy of ±30Pa. The Venturi-tubes were calibrated prior to their installation, and had a calibration of accuracy of ±2%.

The temperatures at the inlet and outlet of the test channel and the coolant channel and the outer wall temperature on the heating plate were measured using sheathed N-type thermocouples with 1mm in diameter. All thermocouples were calibrated prior to their installation. All thermocouples used in the experiments had a calibration accuracy of ±0.3℃.

The pre-heater had a power capacity of 100kW and was able to achieve the appropriate temperature at the inlet of the test channel. The heating plate was directly heated using a DC power supply with a power capacity of 200kW.

All the above mentioned parameters were recorded by a data acquisition system (AT-96) connected to a computer.

4. Single-phase flow and heat transfer

During the experiments, the parameters varied as shown in Table.1. Firstly, the single-phase flow and heat transfer with and without LVG in the channel were discussed to quantitatively learn heat transfer enhancement accompanied by flow drag increase by LV, then the visual velocity and temperature distributions in the two cases were shown to qualitatively explain heat transfer enhancement mechanism related to LV.

Case	With LVG	Without LVG
Thermal boundary	Uniform heat flux on the heating plate	
System pressure	0.25-0.72MPa	0.25-0.72MPa
Mass flow flux	47.5-592.6kg/(m² s)	49.1-669.7kg/(m² s)
Inlet temperature	22.4-88.0℃	23.1-76.4℃
Heat flux	0-201.5kW/m²	0-191.4kW/m²
Reynolds numbers	310-9909	311-9247
Prandtl numbers	4.12-5.27	4.44-5.79

Table 1. Experimental parameters ranges for single-phase flow and heat transfer.

4.1. Flow behavior with and without LVG

It was shown in Fig.7 that the variation of friction factor as a function of Reynolds number in the smooth channel. The laminar-to-turbulent transition occurred at Reynolds number being around 1900. The best fits for data respectively in laminar and turbulent regime as below:

$$f_0 = 176.78 / \mathrm{Re}, \quad \text{where,} \quad \mathrm{Re} < 1900 \tag{6}$$

$$f_0 = 0.3887 / \mathrm{Re}^{0.25}, \quad \text{where,} \quad \mathrm{Re} > 1900 \tag{7}$$

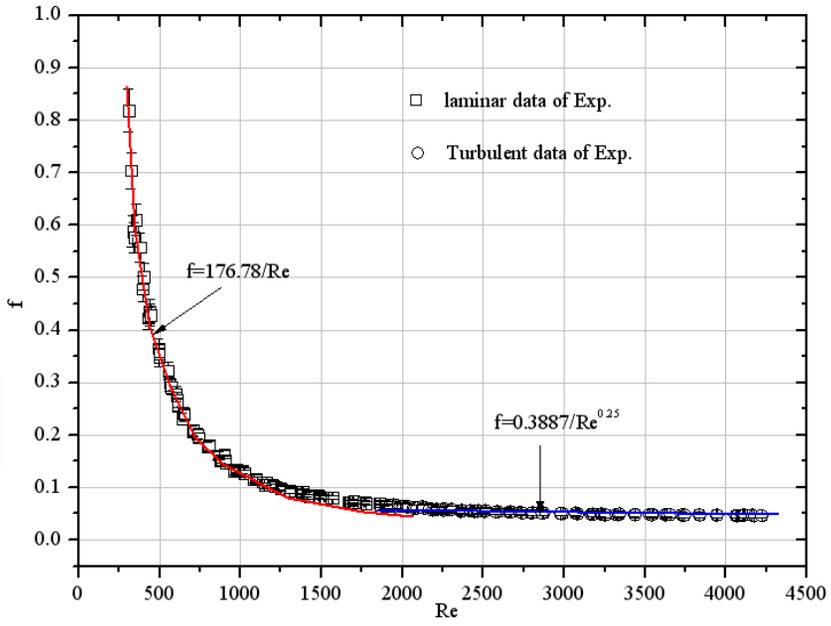

Figure 7. Variation of friction factors with Reynolds numbers in the smooth channel.

It was noticed that, because the channel flow was hydro-dynamically developing, the laminar friction factors were much higher than the corresponding analytical solutions proposed by Kays and Clark (Kays, W.M. & Clark. S.H., 1953), and the turbulent ones were a little higher than the values calculated by Blasius correlation.

In the channel with LVG, the laminar-to-turbulent transition occured at Reynolds number being around 1650, which was shown in Fig.8. The best fits for data respectively in laminar and turbulent regime as below:

$$f = 196.86 / \mathrm{Re}, \quad \text{where,} \quad \mathrm{Re} < 1650 \tag{8}$$

$$f = 0.7786 / \mathrm{Re}^{0.25}, \quad \text{where,} \quad \mathrm{Re} > 1650 \tag{9}$$

In comparison with the smooth channel case, the laminar-to-turbulent transition occurred earlier, and the flow drag became higher in the channel with LVG.

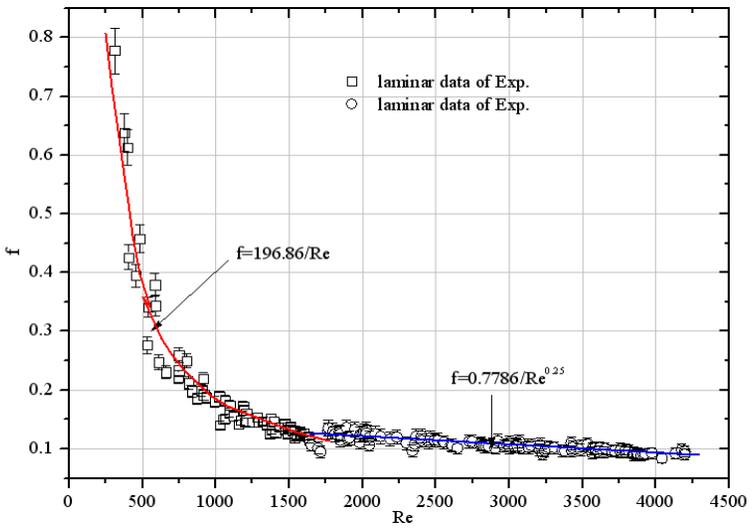

Figure 8. Variation of friction factors with Reynolds numbers in the channel with LVG.

4.2. Heat transfer with and without LVG

It was shown in Fig.9 that the variation of mean Nusselt number as a function of Reynolds number in the smooth channel. The best fits for data respectively in laminar and turbulent regime as below:

$$Nu_0 = 0.0117\,\mathrm{Re}\,\mathrm{Pr}^{1/3}, \quad \text{where,} \quad \mathrm{Re} < 1900 \tag{10}$$

$$Nu_0 = 0.023\,\mathrm{Re}^{0.9}\,\mathrm{Pr}^{0.4}, \quad \text{where,} \quad \mathrm{Re} > 1900 \tag{11}$$

It was also noticed that, because the channel heat transfer was thermally developing and the fluid property varied, the laminar Nusselt numbers weren't constant and were much higher than the corresponding analytical solutions proposed by Shah and London (Shah, R.K. & A.L., 1978), and the turbulent ones were a little higher than the values calculated by Dittus-Boelter correlation.

It was shown in Fig.10 that the variation of mean Nusselt number as a function of Reynolds number in the channel with LVG. The best fits for data respectively in laminar and turbulent regime as below:

$$Nu = 0.0235\,\mathrm{Re}\,\mathrm{Pr}^{1/3}, \quad \text{where,} \quad \mathrm{Re} < 1650 \tag{12}$$

$$Nu = 0.023\,\mathrm{Re}^{0.983}\,\mathrm{Pr}^{0.4}, \quad \text{where,} \quad \mathrm{Re} > 1650 \tag{13}$$

In comparison with the smooth channel case, the heat transfer was enhanced obviously in the channel with LVG.

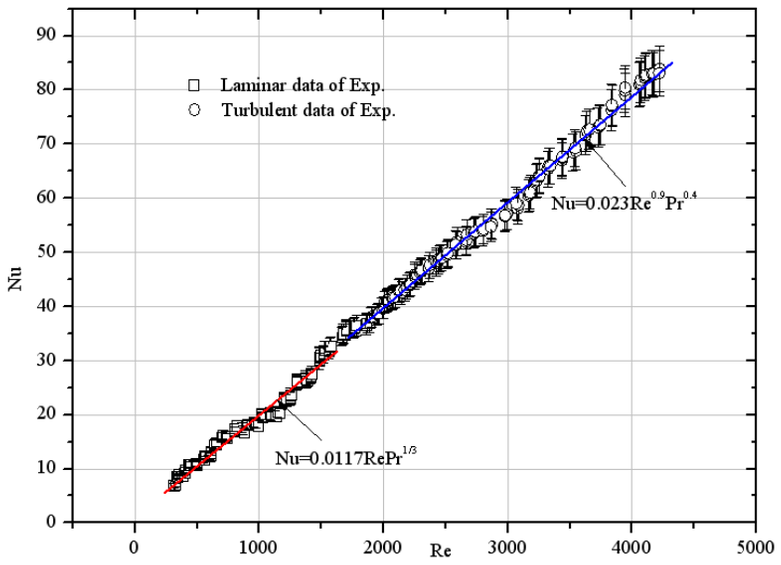

Figure 9. Variation of mean Nusselt numbers with Reynolds numbers in the smooth channel.

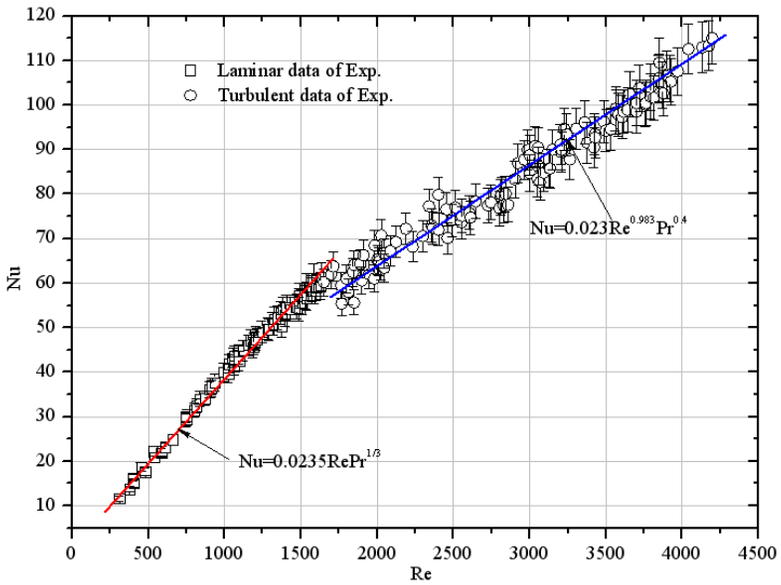

Figure 10. Variation of mean Nusselt numbers with Reynolds numbers in the channel with LVG.

4.3. Evaluation of heat transfer enhancement

Under the conditions of this project, the channel flow and heat transfer in the two cases (with LV and without LV) were thermally and hydro-dynamically developing owing to

entry length effects. With the above discussed, the further interesting results could be introduced.

In the laminar regime with Reynolds numbers lower than 1650, the comparative differences of friction factor and mean Nusselt number between the two different cases were calculated as:

$$\frac{f - f_0}{f_0} \times 100\% = 11.4\% \tag{14}$$

$$\frac{Nu - Nu_0}{Nu_0} \times 100\% = 100.9\% \tag{15}$$

Also, the integral index for evaluating heat transfer enhancement by LV was given as:

$$\frac{Nu / Nu_0}{f / f_0} = 1.8 \tag{16}$$

The above three values indicated that LV could enhance laminar heat transfer up to 100.9% while flow drag increased 11.4% in the test channel, and heat transfer enhancement was 1.8 times against flow drag increase. In a word, the degree of heat transfer enhancement was superior to that of flow drag increase in laminar regime.

In the turbulent regime with Reynolds numbers higher than 1900, the calculated values were as below:

$$\frac{f - f_0}{f_0} \times 100\% = 100.3\% \tag{17}$$

$$\frac{Nu - Nu_0}{Nu_0} \times 100\% = (\mathrm{Re}^{0.083} - 1) \times 100\% > 87.1\% \tag{18}$$

$$\frac{Nu / Nu_0}{f / f_0} = \frac{\mathrm{Re}^{0.083}}{2.003} \tag{19}$$

Therefore, LV could enhance turbulent heat transfer over 87.1% while flow drag increased 100.3% in the test channel, and the heat transfer enhancement to the flow drag increase ratio was a power law function of Reynolds numbers, and the performance of heat transfer enhancement would become better with increase Reynolds numbers in turbulent regime.

4.4. Velocity distribution with and without LVG

To learn LV's behavior related to flow drag increase, a Phase Doppler Particle Analyzer (PDPA) was employed to measure velocity distribution in the two different channels. Each measuring plane was perpendicular to the channel axial direction; the measuring coordinates and data acquisition dots were shown in Fig.11.

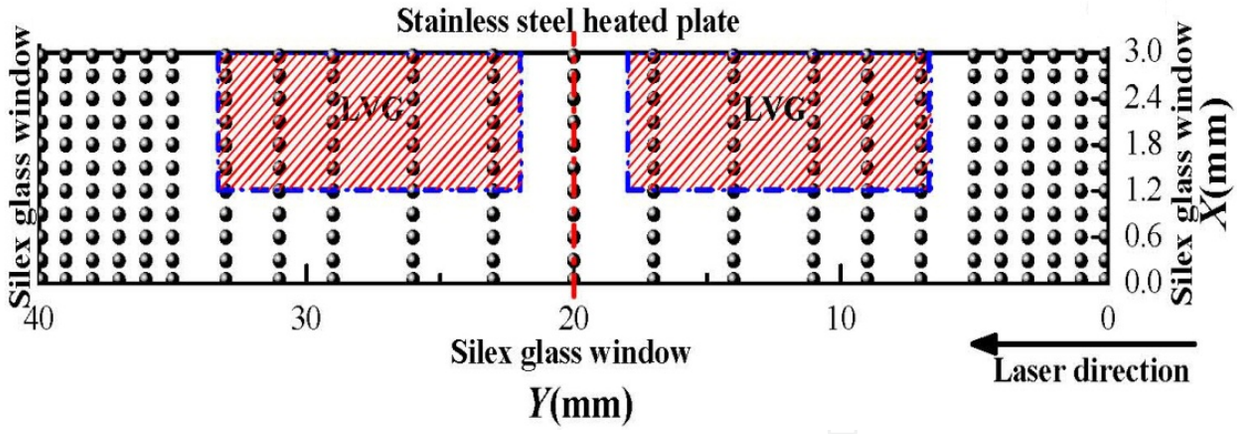

Figure 11. Schematic of measuring coordinates and data acquisition dots using PDPA

The first measuring plane was located at Z=65mm in the axial direction and was 15mm far from the front corners on the first pair of ribs. The data measured in the two different cases were shown in Fig.12. It was seen that LVG caused the normal velocity distribution distort (still symmetrical) at different locations. This phenomenon indicated that the LVG could produce LV and reconstruct velocity field in the channel. In Fig.12(a), a stagnation domain formed immediately behind the ribs, the bulk velocity decreased, and the boundary layer became thicker; when moving downstream, LV was stronger because of upstream superimposition. In Fig.12(b) and Fig.12(c), the wall effect became weaker, the bulk velocity increased, the boundary layer became thinner, and the bulk velocity in the channel with LVG was bigger than that in the smooth channel. During moving downstream, LV swirled from channel center to both sides in an involute path, thus exhibited strong three-dimensional characteristics. In comparison with the case of smooth channel, the form drag was the reason for flow drag increase in the channel with LVG.

4.5. Temperature distribution with and without LVG

To learn LV's behavior related to heat transfer enhancement, a thermal infrared imager was employed to measure outer wall temperature distribution in the two different channels. The measuring region was on the heating plate where the tail two pairs of ribs were against the empty space.

The comparison of measuring images from the two different cases was shown in Fig.13. In the smooth channel, the outer wall temperature distribution was homogeneous, which was coincidence with the thermal characteristics under constant heat flux wall boundary. In the channel with LVG, the symmetrical lower temperature region formed immediately behind the ribs, and periodically appeared and disappeared in the axial direction. This phenomenon indicated that LV could reconstruct temperature field and improve local heat transfer capability periodically in the channel.

The more accurate result was shown in Fig.14. It could be found that the mean outer wall temperature in the channel with LVG was lower than that in the smooth channel by 18.1%. Therefore, LV could obviously enhance heat transfer in the channel.

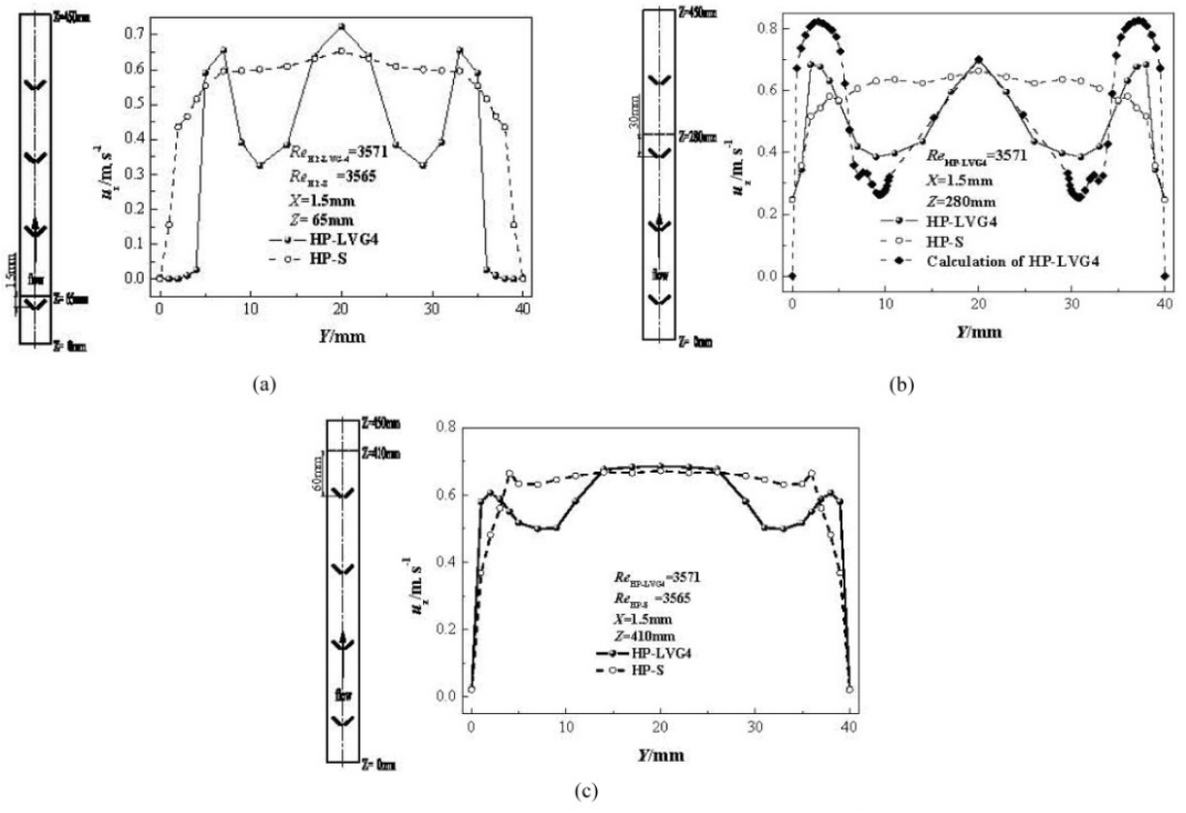

Figure 12. Comparison of velocity distribution in the two cases.(p_{in}=0.465Mpa, u_{in}=0.493m/s, and T_{in}=23.3℃)

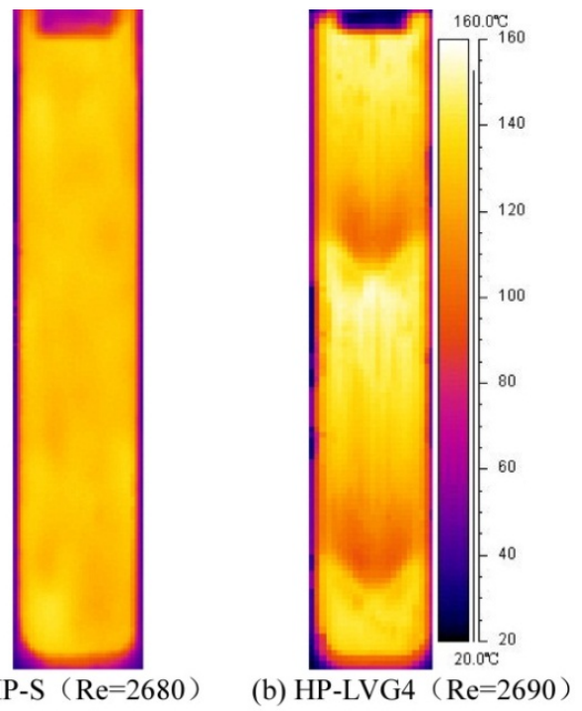

Figure 13. Outer wall temperature fields in the two cases in turbulent flow

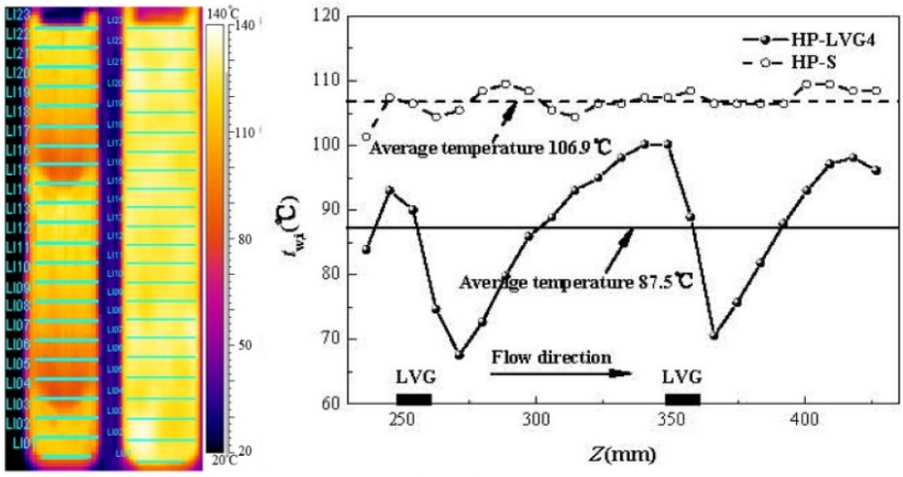

Figure 14. Quantitative comparison of wall temperature between the two cases.(p_{in}=0.461MPa, G=435.9kg/(m²·s), $T_{l,m}$=34.1℃,and q=240.9kW/m²)

5. Vapor-liquid two-phase flow and heat transfer

During the experiments, the parameters varied as shown in Table.2. Firstly, bubble behaviors with and without LVG in the channel were observed to learn the two-phase heat transfer enhancement accompanied by flow drag increase, then two-phase flow and heat transfer in the two cases was discussed.

Case	With LVG	Without LVG
Thermal boundary	Uniform heat flux on the heating plate	
System pressure	0.44-0.81MPa	0.45-0.82MPa
Mass flow flux	65.9-415.9kg/(m² s)	50.7-330.4kg/(m² s)
Inlet temperature	93.6-120.8℃	93.2-128.1℃
Heat flux	8.7-885.9kW/m²	7.0-834.6kW/m²
Reynolds numbers	1353-7364	1596-6758
Prandtl numbers	1.23-1.57	1.25-1.73

Table 2. Experimental parameters ranges for two-phase flow and heat transfer.

5.1. Bubble behaviors with and without LVG

In order to learn LV behavior related to two-phase flow drag increase, a high-speed camera was employed to record bubble behaviors in the two different cases, and the measuring region contained all the four pairs of ribs. It was shown in Fig.15 that the bubble evolve between z=45mm and z=75mm near the first pair of ribs, where Onset of Nucleate Boiling (ONB) began to appear. Obviously, the number of bubbles attached on the wall was small, and bubbles mainly distributed in both sides and the central region of the channel; this phenomenon could be ascribed to the bubble production being small and LV stir. The arrowed line denoted the dominant region by LV. In this region, bubbles couldn't

congregate on the wall, but moved downstream with bulk fluid, thus the heat transfer capability between the cold and hot fluid was improved.

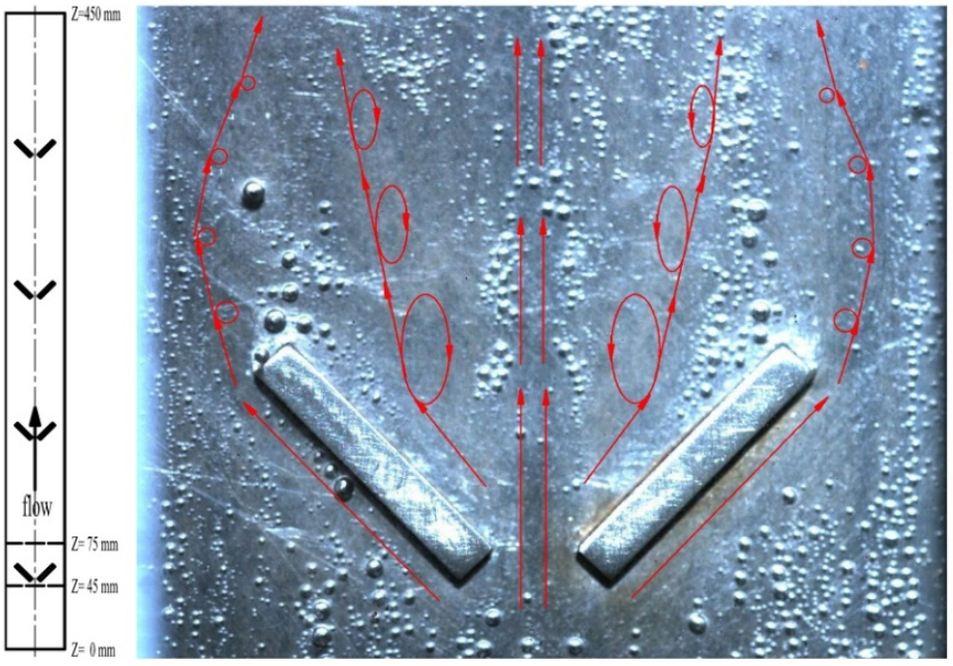

Figure 15. Bubbles distribution near the first pair of ribs in the channel with LVG.(pin=0.507MPa, G=413.6kg/(m² • s), ΔTsub=44.6℃,and q=296.7kW/m²)

It was illustrated respectively in Fig.16 and Fig.17 that the bubbles evolve with heat flux increase in the two different cases. In the smooth channel, a huge number of coalescent bubbles moved downstream without transverse stir. In the channel with LVG, the number of bubbles obviously decreased a lot, the bubble transverse stir was stronger, the bubble growth was inhibited, and bubbles weren't easy to coalesce, thus more heat on the heated surface was transferred. As being bounded in narrow gap, distorted bubbles almost occupied the whole space in the transverse direction; the big bubbles directly pushed superheated liquid layer depart from the wall surface; the small ones were baffled by these slow rising big bubbles and moved around; a single bubble couldn't exist; a large number of bubbles coalesced and improved vapor quality. All of this facilitated the two-phase mixture to speed up. Therefore, the bubble departure diameter became smaller while the bubble growth frequency became higher, and the bubble stir was strengthened, which was one of the important factors for boiling heat transfer enhancement.

5.2. Two-phase friction pressure drop with and without LVG

Two-phase friction pressure drop was an important hydrodynamic parameter to measure flow drag increase in channel flow. In this study, the two-phase friction pressure drop in the channels was most dependent on the exit quality in all related parameters. The best fits for two-phase friction pressure drops in the two different channels were listed as the following correlations:

$$\Delta p_{\mathrm{f,smooth}} = 3959.118\left(-3.664x^2 + 3.409x + 0.020\right)^{1.919} \tag{20}$$

$$\Delta p_{\mathrm{f,LVG}} = 1100.514\left(171.642x^2 - 7.266x + 0.168\right)^{0.277} \tag{21}$$

where x denoted the channel exit quality and varied between 0.179 and 0.6. The predicted results by the two equations deviated to the corresponding experimental data by ±30%, which was shown in Fig.18.

It was calculated using Eq.(20) and Eq.(21) that the two-phase friction pressure drop ratio between the two cases was 1.04-1.506, or the value in the channel with LVG .

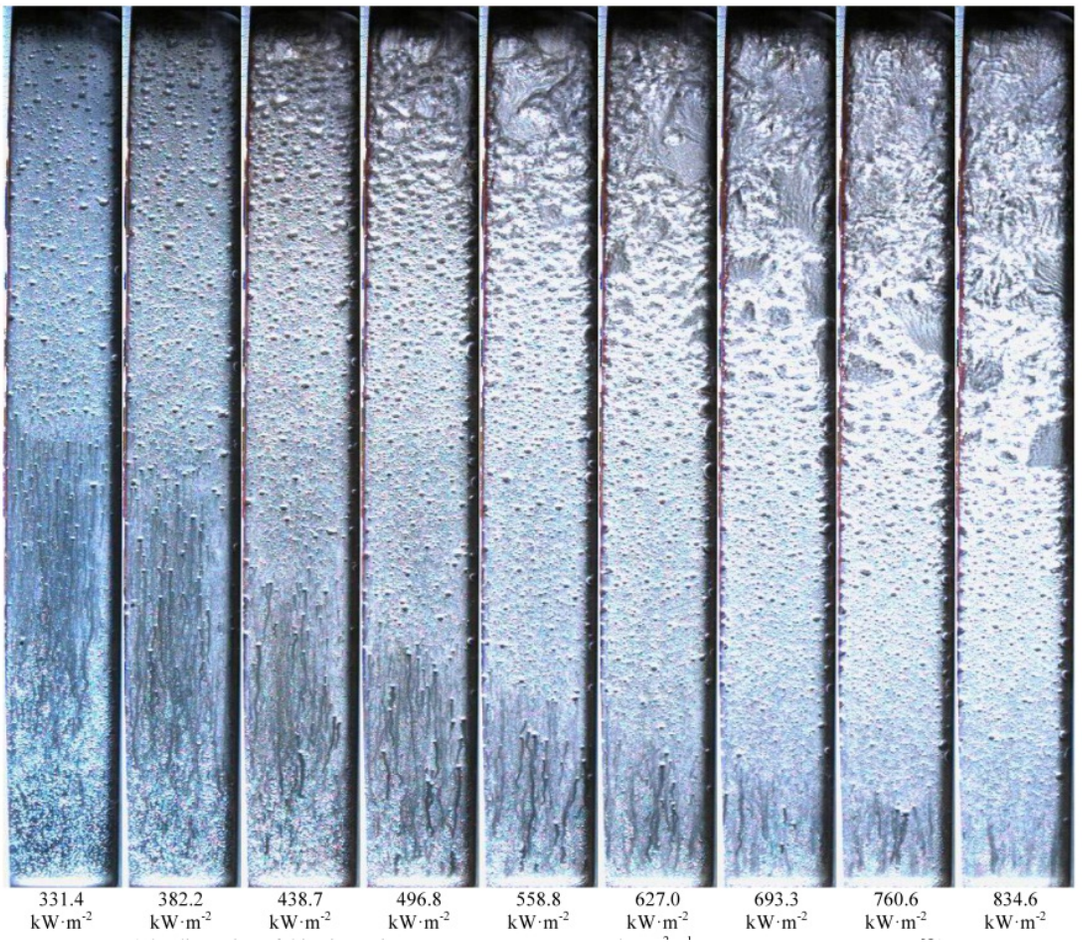

Figure 16. Bubbles evolution with heat flux increase in the smooth channel.(pin=0.620MPa, G=270.7kg/(m² • s), and ΔTsub=57.9℃)

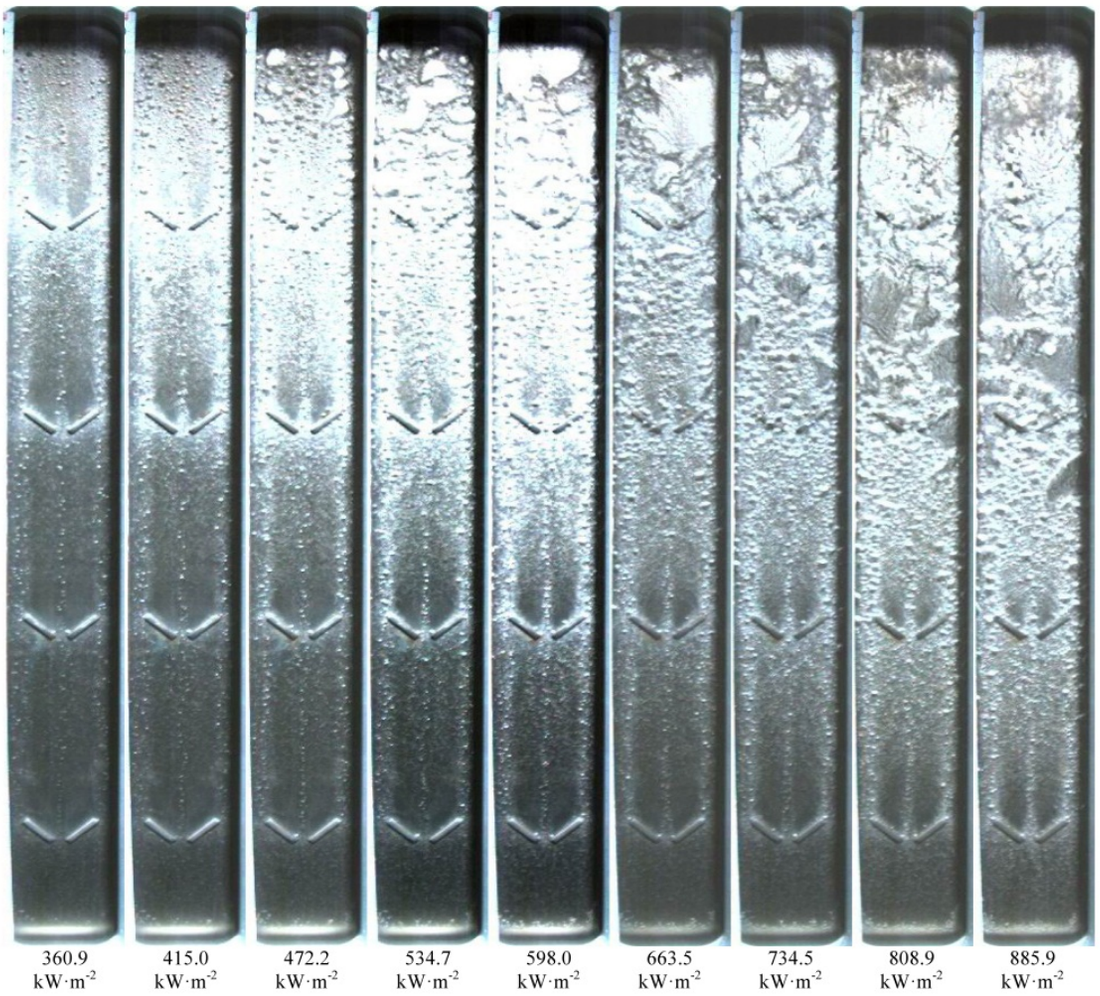

Figure 17. Bubbles evolution with heat flux increase in the channel with LVG.(pin=0.654MPa, G=278.9kg/(m2・s), and △Tsub=58.2℃)

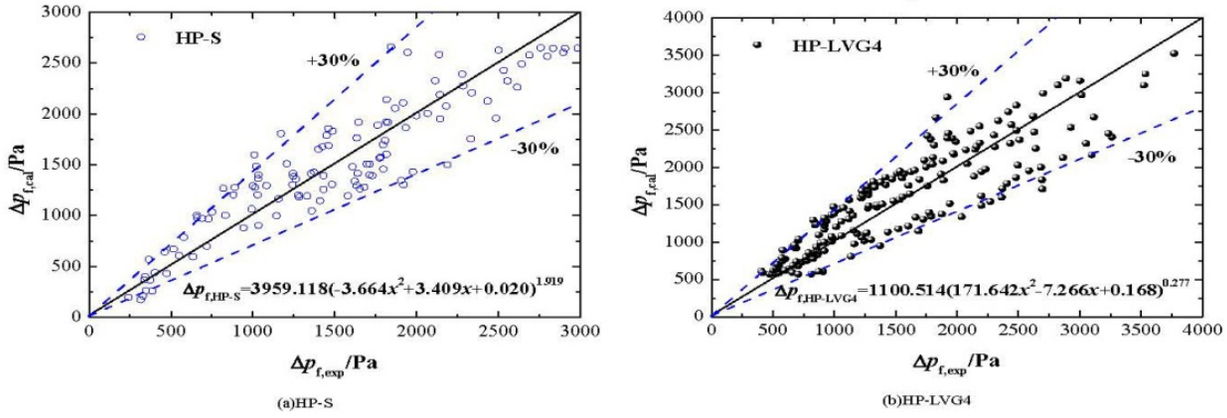

Figure 18. Friction pressure drop comparison between prediction and experiment in the two cases.

5.3. Two-phase boiling heat transfer with and without LVG

In this study, the two-phase boiling heat transfer behavior was discussed. The heat transfer coefficients were correlated with Reynolds number, Boiling number, thermal conductivity and hydraulic diameter by taking the form proposed by Gungor and Winterton(Gungor K.E., Winterton R.H.S., 1987), which was adaptable to narrow rectangular channel with a big aspect ratio. The best fits for heat transfer coefficient in the two different channels were listed as below:

$$h_{\mathrm{TP,without\,LVG}} = 1.40 Re \cdot Bo^{0.349} \lambda / D_{\mathrm{hy}} \tag{22}$$

$$h_{\mathrm{TP,with\,LVG}} = 3.05 Re \cdot Bo^{0.440} \lambda / D_{\mathrm{hy}} \tag{23}$$

where the Reynolds number varied between 1596 and 6758, and the Boiling number varied between 2.15×10^{-4} and 2.137×10^{-3}.

The prediction by the two equations deviated to the corresponding experimental data by ±30%, which was shown in Fig.19.

It was calculated using Eq.(22) and Eq.(23) that the two-phase boiling heat transfer coefficient ratio between the two cases was 1.011-1.258, or the value in the channel with LVG was 1.1%-25.8% higher than that in the smooth channel.

6. Critical Heat Flux

In this section, CHF with and without LVG in the test channel was intentionally studied. Firstly, the observation of bubble and liquid film behaviours was conducted when CHF occurred in the two different channels; then the quantitative CHF in the two cases was discussed especially in the parameter dependence and experimental correlations; finally the analytical models for CHF in the two cases were proposed and validated. The varied parameters during the experiment were listed in Table.3.

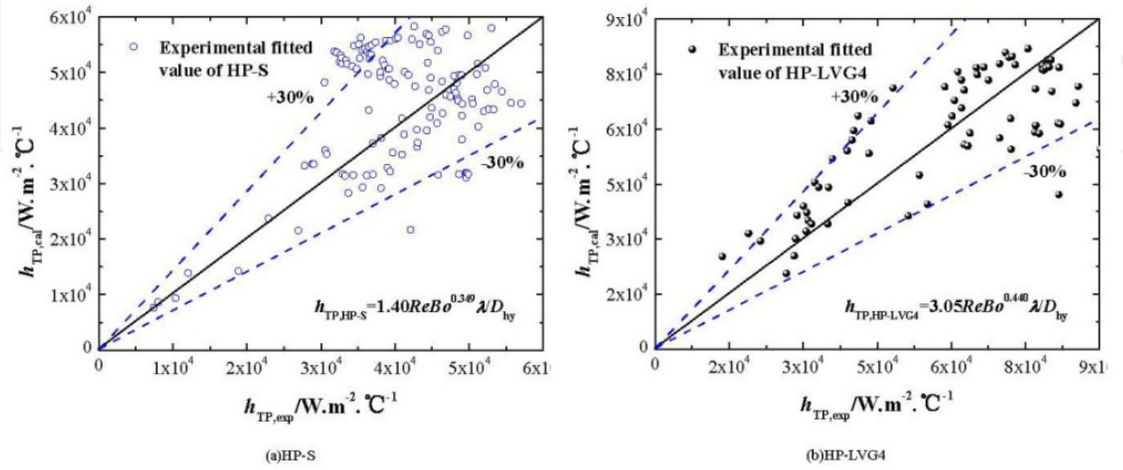

Figure 19. Boiling heat transfer coefficient comparison between prediction and experiment in the two cases.

Case	With LVG	Without LVG
Thermal boundary	Uniform heat flux on the heating plate	
System pressure	0.43-0.85MPa	0.44-0.82MPa
Mass flow flux	40.2-690.1kg/(m²s)	40.2-745.7kg/(m²s)
Subcooling	46.8-104.2℃	51.7-100.2℃
Quality	0.203-1.000	0.183-0.997
CHF	0.299-2.316MW/m²	0.294-2.263MW/m²

Table 3. Experimental parameters ranges for CHF experiments

6.1. Bubble and liquid film behaviours

In order to learn LV's behaviour during CHF occurrence, the high-speed camera was employed to record bubble behaviours in the two different cases, and the measuring region contained all the four pairs of ribs.

By comparison between Fig.20 and Fig.21, it was found that ONB in the channel with LVG appeared later than that in the smooth channel when CHF occurred. The main reason for this phenomenon was that the bubbles growth was inhibited by LV, and the number of bubbles decreased with the generation of LV, and the bubbles were very difficult to coalesce under LV dominance. Simultaneously, the disturbance of liquid film on the wall in the channel with LVG was much stronger than that in the smooth channel. As a result, CHF was greatly improved with the help of LV.

In more details, it was found in Fig.22 that the void fraction increased in the axial direction, and the transverse distribution of vapour-phase varied under LV dominance. The channel flow and heat transfer would greatly change with such heterogeneousness. First of all, the disturbance of bubbles, energy transfer and momentum transfer in the channel were all strengthened by LV. Secondly, the bubbles growth and coalescence were inhibited by LV, also the bubbles collision frequency was low. Thirdly, the enhanced bubbles disturbance facilitated to destroy thermal boundary layer. Finally, the bubbles would be brought from the side wall to the central region by LV. All these factors would help improve heat transfer and CHF in the channel.

On the one hand, it was shown in Fig.20 that CHF in the smooth channel occurred at the moment of 0.380s, prior to which, the wall surface had been covered with a layer of stable liquid film. When CHF occurred, the liquid film began to lose stability owing to the rapid pressure drop variation with heat flux, though the heating power had been cut down by 50%. On the other hand, Fig.21 showed that CHF in the channel with LVG occurred at the moment of 0.400s, prior to which, the liquid film had been disturbed by LV. This phenomenon was beneficial to accelerate the liquid film evaporation, thus more energy was transferred, and CHF was improved.

It was also seen in Fig.22 that liquid film evolved near the fourth pair of ribs during CHF occurrence, the vapour-phase occupied the channel central region while the liquid-phase

concentrated on the side wall, and thus a typical annular flow pattern came into being. Under LV dominance, the liquid film distribution became heterogeneous on the wall surface, and the wall temperatures fluctuated periodically, while annular flow and slug flow alternately appeared in the channel. Such a reverse flow pattern transition visually indicated CHF enhancement in the channel with LVG.

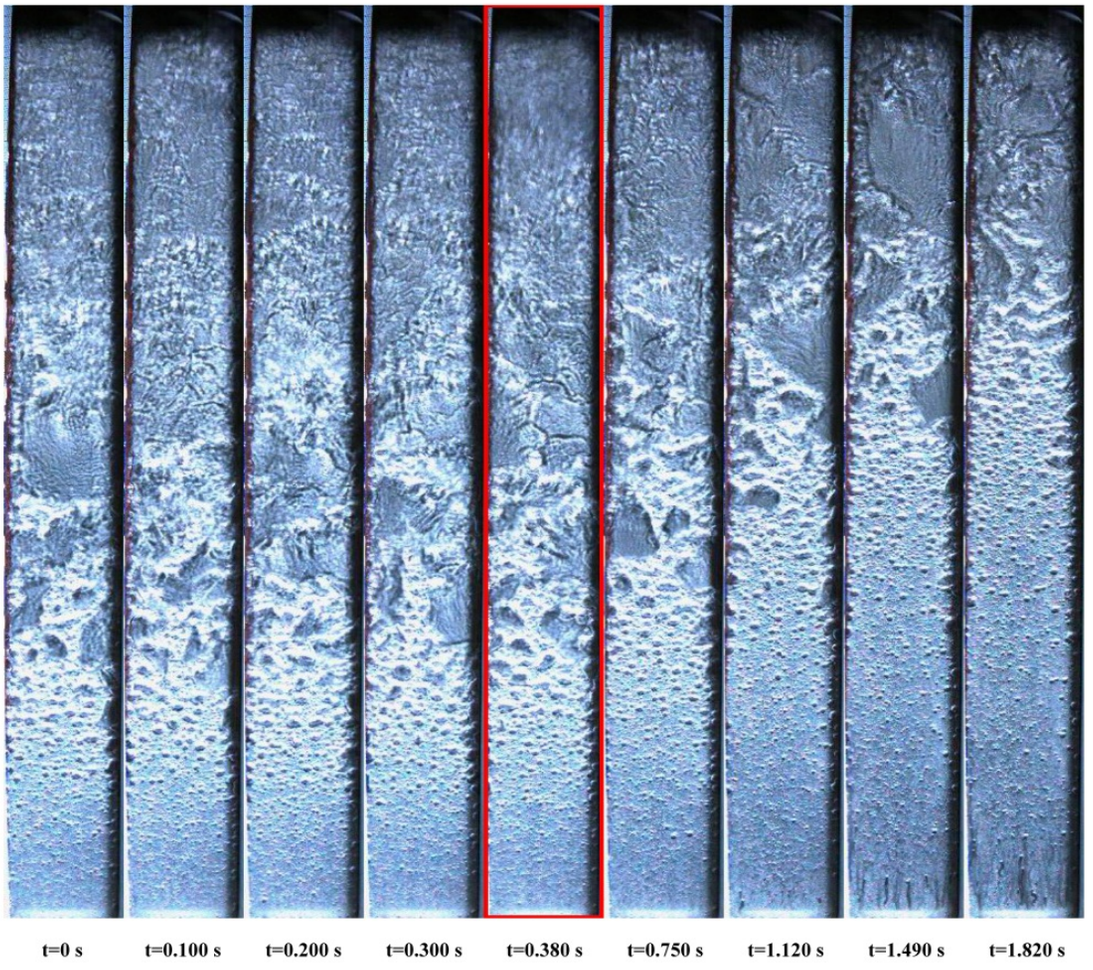

Figure 20. Bubble evolution during CHF occurrence in the smooth channel. (pin=0.713MPa, G=217.1kg/(m2・s), ΔTsub=52.1℃,and qc=1.287MW/m2)

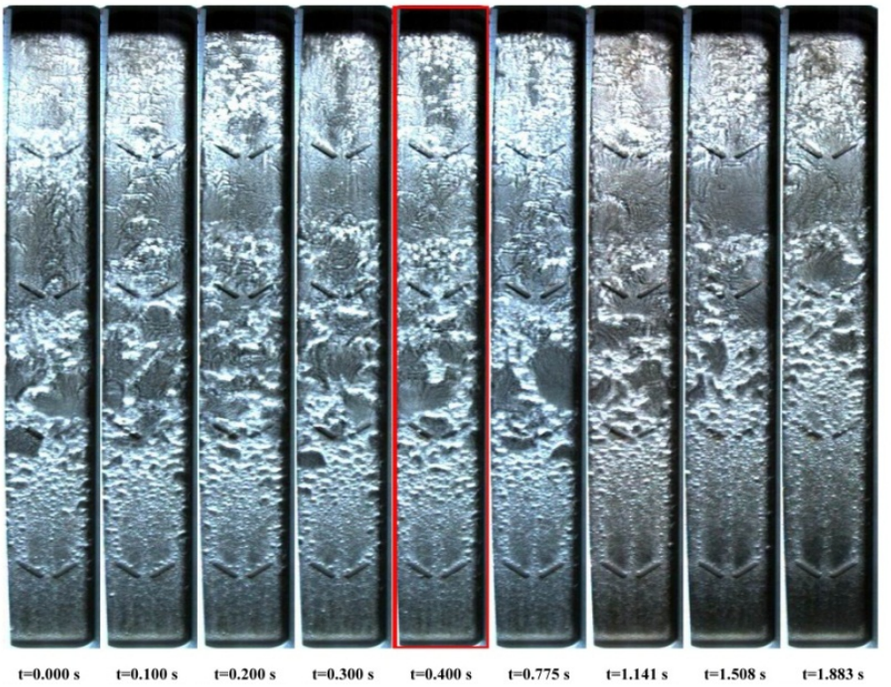

Figure 21. Bubble evolution during CHF occurrence in the channel with LVG. (pin=0.763MPa, G=198.9kg/(m2・s), ΔTsub=61.4℃, and qc=1.327MW/m2)

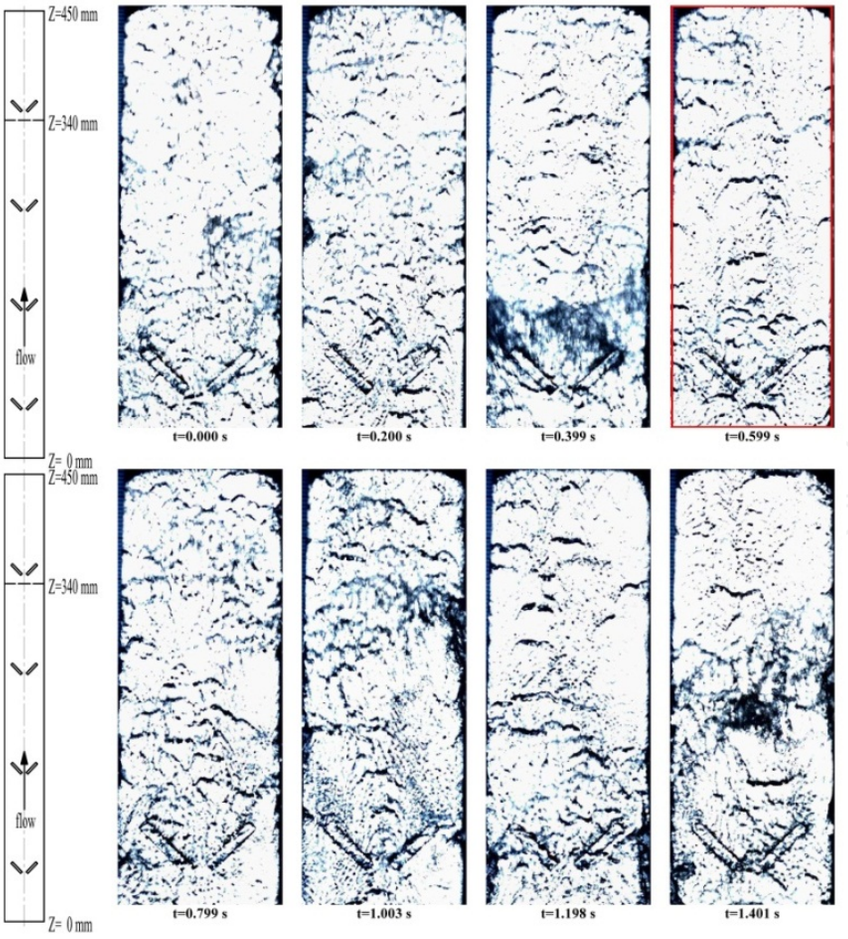

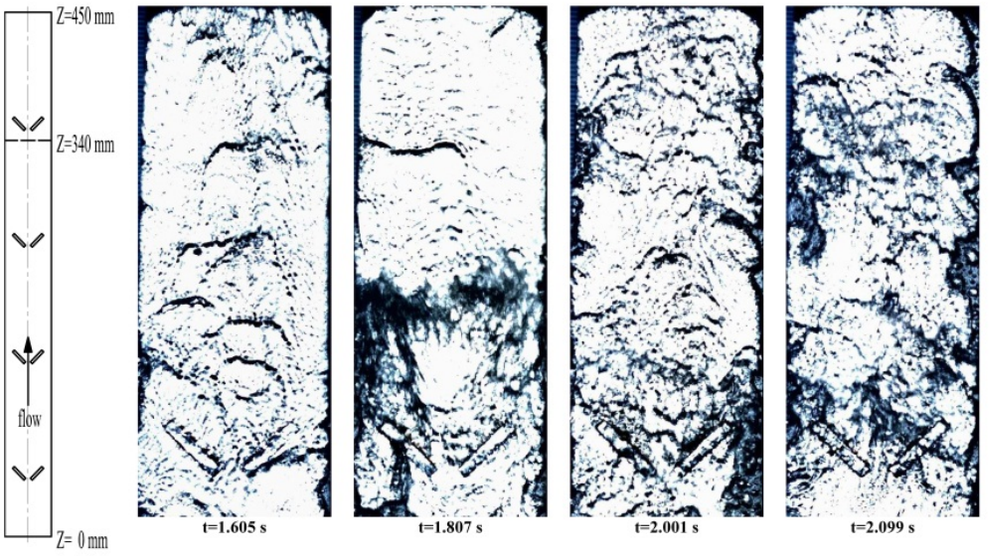

Figure 22. Liquid film evolution during CHF occurrence near the fourth pair of ribs in the channel with LVG. (pin=0.663MPa, G=188.2kg/(m2・s), ΔTsub=53.1℃, and qc=1.238MW/m2)

6.2. Parameter dependence and experimental correlations

By reduction on experimental data, it could be found in Fig.23 that the CHF value varied with different parameters in the two different channels. In these two cases, the CHF value monotonously decreased with exit quality increase, and monotonously increased with mass flow flux and pressure drop increase, but had no obvious variation with system pressure and inlet subcooling. It seemed that the difference between the two cases was difficult to find, therefore, the more detailed discussion needed to be conducted.

Taking the above mentioned parameter dependence into consideration, the best fits for CHF in the two cases were obtained as below:

$$q_{\mathrm{c,smooth}} = \left(0.0022G - 0.0767\right)^{0.5002}\left(0.0005\Delta t_{\mathrm{sub,in}} + 0.6695\right)^{1.6000} \times \left(-10.9828p_{\mathrm{in}}^2 + 15.9420p_{\mathrm{in}} - 1.9973\right) \quad (24)$$

$$q_{\mathrm{c,LVG}} = \left(0.0315G - 0.7638\right)^{0.5385}\left(0.0142\Delta t_{\mathrm{sub,in}} - 0.4344\right)^{0.2413} \times \left(-1.9409p_{\mathrm{in}}^2 + 2.9748p_{\mathrm{in}} - 0.5006\right) \quad (25)$$

The prediction by the two equations deviated to the corresponding experimental data by ±10%, which was shown in Fig.24.

It was calculated using Eq. (24) and Eq. (25) that the CHF value in the channel with LVG was 24.3% higher than that in the smooth channel within the present experimental parameter range.

Also, the best fits for pressure drop in the two cases were obtained as below:

$$\Delta p_{\mathrm{c,smooth}} = \left(2.1854G - 46.0350\right)^{0.5842}\left(-1.0776\Delta t_{\mathrm{sub,in}} + 165.4139\right)^{0.3839} \times\left(-216.8849p_{\mathrm{in}}^{2} + 278.0483p_{\mathrm{in}} - 49.6720\right) \tag{26}$$

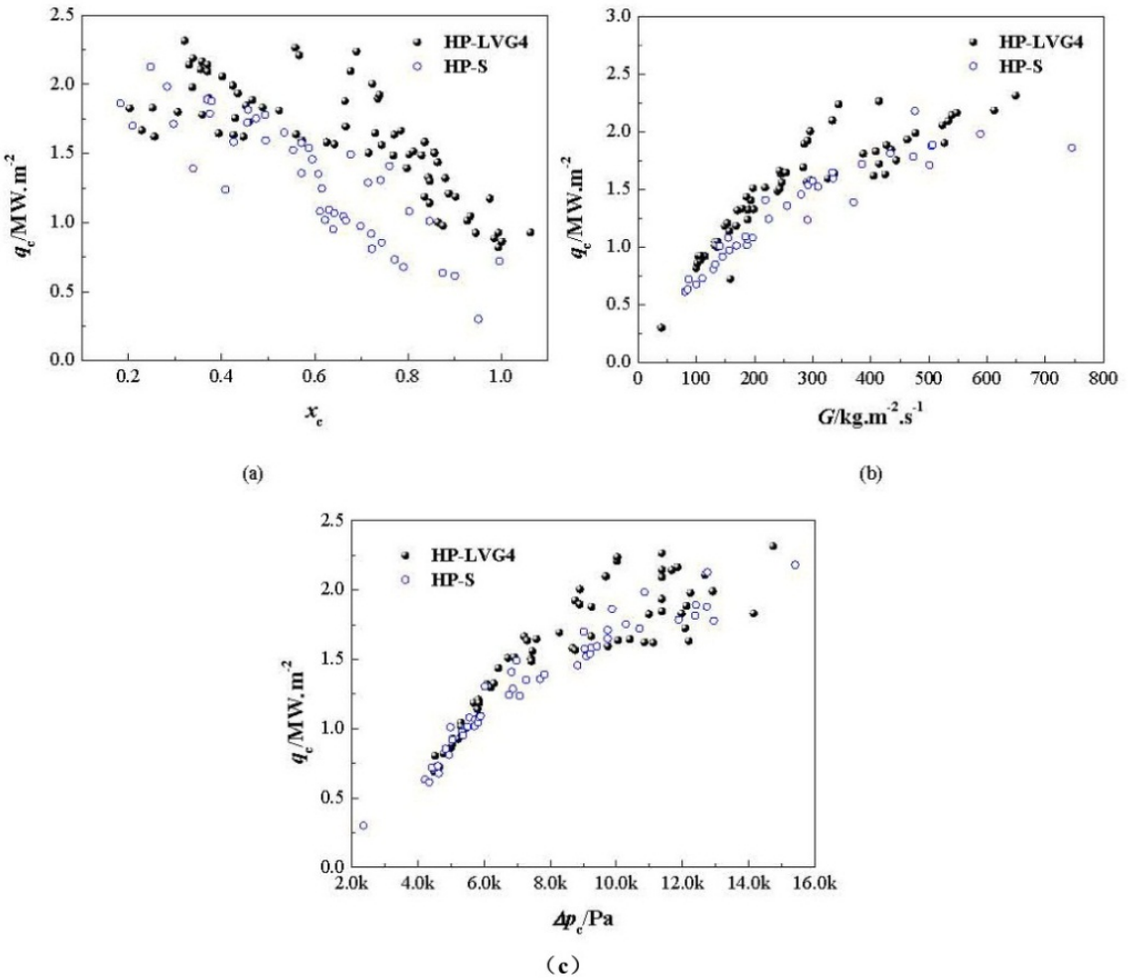

Figure 23. CHF variation with several thermal-hydraulic parameters in the two channels

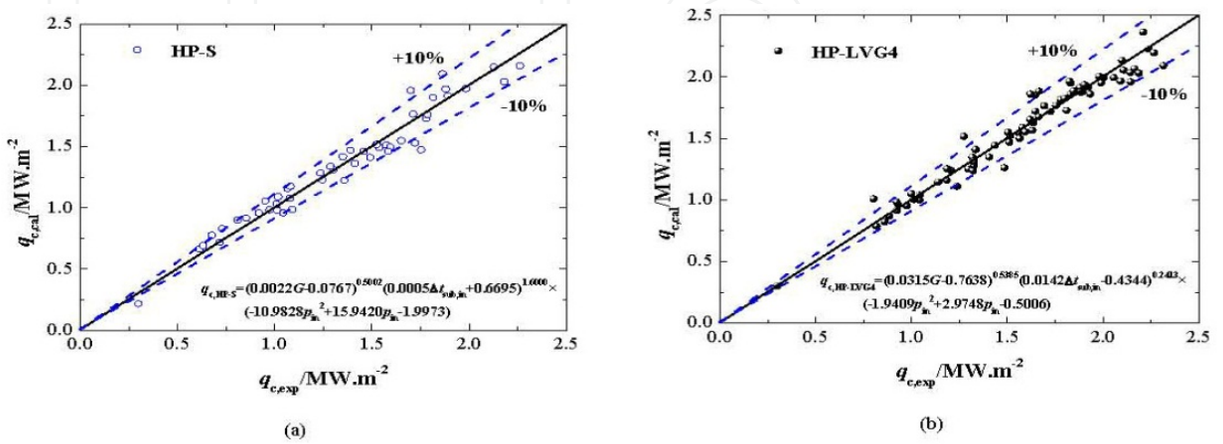

Figure 24. Comparison between the experimental data with the predicted values of CHF in the two channels.

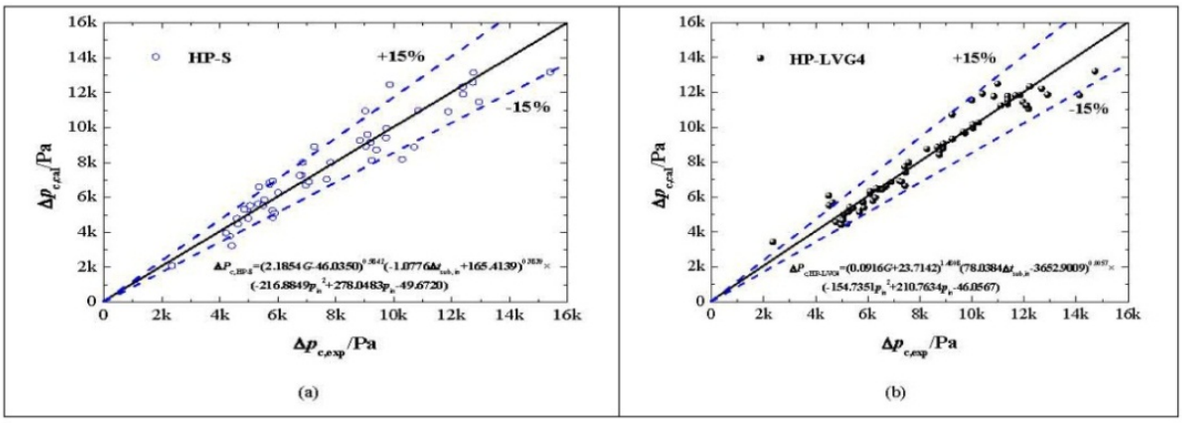

Figure 25. Comparison between the experimental data with the predicted value of pressure drops in the two channels.

$$\Delta p_{\mathrm{c,HP\text{-}LVG4}} = \left(0.0916G + 23.7142\right)^{1.4808}\left(78.0384\Delta t_{\mathrm{sub,in}} - 3652.9009\right)^{0.0057} \times\left(-154.7351p_{\mathrm{in}}^2 + 210.7634p_{\mathrm{in}} - 46.0567\right) \tag{27}$$

The prediction by the two equations deviated to the corresponding experimental data by ±15%, which was shown in Fig.25.

It was calculated using Eq. (26) and Eq. (27) that the pressure drop value in the channel with LVG was 62.9% higher than that in the smooth channel within the present experimental parameter range.

Obviously, the CHF increase must be at the cost of pressure loss in the channel with LVG, which well followed the second thermodynamic law.

6.3. Analytical models for CHF

CHF is a vital parameter for Nuclear Reactor Design and operation. Up to now, a large number of experimental investigations have been conducted for different channel type, and a large amount of experimental data and correlations have been obtained. However, the applicability of these data based correlations is strictly limited by experimental parameters. Analytical model for CHF is encouraged due to its advantages on physical mechanism and applicability.

The annular flow liquid film dry-out mechanism for CHF (Joel, 1992) has been known very well. Fig.26 exhibited the CHF occurrence process related to this mechanism. Owing to the simultaneous effects from the droplet deposition, droplet entrainment, and liquid film evaporation, the liquid film on the wall surface become more and more thin and even disappear, CHF will occur at some point. On the basis of this mechanism, the multi-fluid model for CHF had been proposed, but the modelling was complicated as too many field equations need to be solved. In addition, several constitutive correlations were not accurate enough because the studies on two-phase interface transfer had been still premature. On the contrary, Celata and Zummo's analytical model incorporated the appropriate droplet deposition and

entrainment, and was able to predict the CHF in annular flow with a comparative high accuracy, therefore the analytical model for CHF in this project will refer to this model.

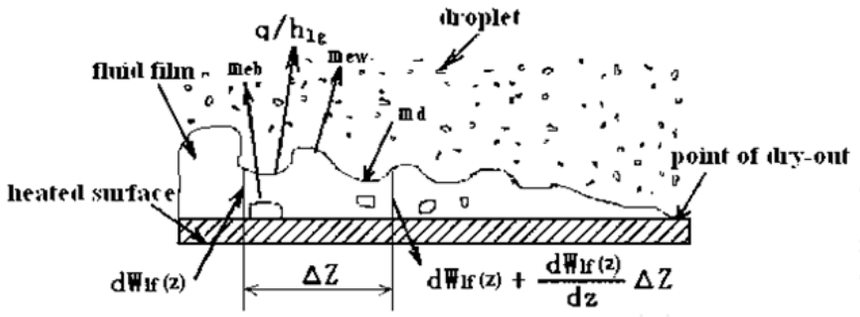

Figure 26. Schematic of liquid film dry-out mechanism of annular flow in narrow rectangular channel.(m_d, m_{ew}, m_{eb}, and q/h_{lg} were droplet deposition rate, vapour stream shear caused droplet entrainment rate, broken bubble-caused droplet entrainment rate and liquid film evaporation rate, respectively.)

Despite that the flow patterns and CHF analytical model for narrow rectangular channel had been difficult to find in open literature, several researchers (Jackey, et al., 1958; Kafengauz and Bocharov, 1959) suggested that the correlations for CHF in conventional pipe could be used for the case in narrow rectangular channel if the equivalent characteristics scale was same, which was shown in Fig.27.

6.3.1. Onset of annular flow

Mishima and Ishii's (1984) criterion was employed to predict the onset of annular flow in the present cases:

$$j_g \geq \left(\frac{\sigma g \Delta\rho}{\rho_g^2}\right)^{0.25} \Big/ \left[\mu_l\left(\rho_l \sigma \sqrt{\frac{\sigma}{g\Delta\rho}}\right)^{-0.5}\right]^{0.2} \tag{28}$$

Eq.(28) was tenable in the range as following: pressure between 0.1Mpa and 20.0 MPa, mass flow flux between 8 kg/(m²·s) and 15,000 kg/(m²·s), channel equivalent diameter between 0.001m and 0.025 m, channel length to equivalent diameters ratio between 1 and 400, inlet subcooling between 10◎ and 255◎, and exit quality between 0.1 and 1.

6.3.2. Mass flow rate of liquid film in annular flow region

If annular flow appeared in the channel, the onset location (z_{on}) could be obtained, and the mass flow rate of liquid film was calculated by Eq. (36) integral between the onset location and the channel outlet.

$$\frac{dW_{lf}}{dz} = \pi D_{hy}\left(m_d - m_{ew} - m_{eb} - \frac{q}{h_{lg}}\right) \tag{29}$$

The droplet deposition rate was calculated using Kaotaoka and Ishii's (1983) correlation.

$$m_{\mathrm{d}} = 0.22 Re_{\mathrm{l}}^{0.74} E^{0.74} \left(\frac{\mu_{\mathrm{g}}}{\mu_{\mathrm{l}}} \right)^{0.26} \frac{\mu_{\mathrm{l}}}{D_{\mathrm{hy}}} \tag{30}$$

where R_{el} was the liquid-phase Reynolds number; E was the droplet entrainment fraction in the channel cross section, and was calculated as below:

$$E = 1 - \frac{j_{\mathrm{lf}}}{j_{\mathrm{l}}} \tag{31}$$

where the superficial liquid film velocity was calculated as below:

$$j_{\mathrm{lf}} = \frac{4W_{\mathrm{lf}}}{\rho_{\mathrm{l}} \cdot \pi \cdot D_{\mathrm{hy}}^2} \tag{32}$$

Owing to the mass flow rate W_{lf} was an unknown quantity in Eq. (32), an iteration method was used to calculate E.

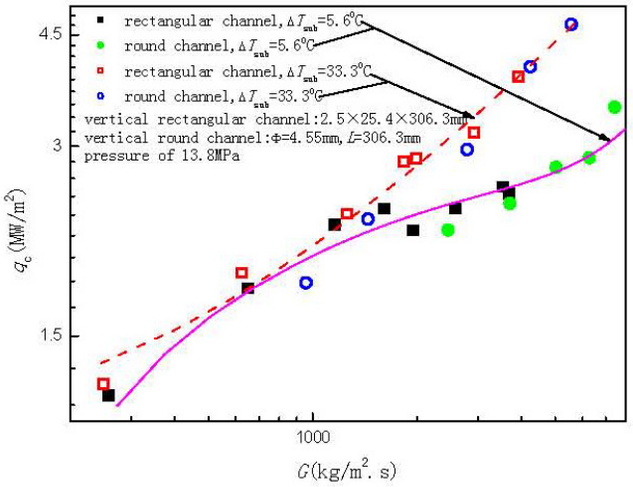

Figure 27. Critical heat flux trend of different type of channels with identical equivalent diameter

6.3.3. Droplet entrainment rate

(1) Broken bubble caused droplet entrainment

In this case, Ueda et al. (1981) correlation was used to calculate the droplet entrainment rate.

$$m_{\mathrm{eb}} = 477 \left[\frac{q^2 \delta}{h_{\mathrm{lg}}^2 \sigma \rho_{\mathrm{g}}} \right]^{0.75} \frac{q}{h_{\mathrm{lg}}} \tag{33}$$

Where liquid film thickness δ was calculated by iteration from Eq. (34) to Eq. (37).

$$U_{\mathrm{lf,m}}^{+} = \frac{\int U^{+} dY^{+}}{\delta} \tag{34}$$

$$U_{\mathrm{lf,m}} = \frac{G_{\mathrm{lf}}}{A_{\mathrm{lf}}\rho_{\mathrm{l}}} \tag{35}$$

$$U^{+}_{\mathrm{lf,m}} = \frac{U_{\mathrm{lf,m}}}{\sqrt{\frac{\tau_{\mathrm{w}}}{\rho_{\mathrm{l}}}}} \tag{36}$$

$$A_{\mathrm{lf}} = \frac{D^2_{\mathrm{hy}}}{D^2_{\mathrm{hy}} - \left(D_{\mathrm{hy}} - 2\delta\right)^2} \tag{37}$$

(2) Vapour stream shear caused droplet entrainment

In this case, Kaotaoka's (1983) correlation was used to calculate the droplet entrainment rate.

$$m_{\mathrm{ew}} = 0.22 Re_{\mathrm{l}}^{0.74} E_{\infty}^{0.74} \left(\frac{\mu_{\mathrm{g}}}{\mu_{\mathrm{l}}}\right)^{0.26} \frac{\mu_{\mathrm{l}}}{D_{\mathrm{hy}}} \tag{38}$$

where E_{∞} was equilibrium droplet fraction and was calculated as below:.

$$E_{\infty} = \tanh\left(7.25 \times 10^{-7} We^{1.25} Re^{0.25}\right) \tag{39}$$

where We is the Weber number.

The iteration process for CHF calculation was depicted as: Eq. (28) is used to estimate whether annular flow appear or not. If the supposed CHF was lower than the actual value, annular flow will not appear; contrarily, this flow pattern will appear. After the onset location (z_{on}) of annular flow being obtained, the parameters m_d, m_{ew}, m_{eb}, and W_{lf} were calculated at each time step from z_{on} to the channel outlet; if the supposed heat flux was lower than CHF, the mass flow rate of liquid film was over zero at the outlet; contrarily, this mass flow rate became zero before the outlet; the iteration finished until the supposed heat flux was equal to CHF.

6.3.4. The assessment of the model

Based on the analytical model, a computer code had been developed in FORTRAN language. The total fifty-seven groups of experimental CHF data in the smooth channel were used to validate the model. The validated result was shown in Fig.28. It was seen that 93% of prediction data fell within ±30% of discrepancy band. In general, the model had a good accuracy, and it could be used to predict CHF in the smooth channel.

The prior study (Wang L. & Wang Q.W., 2005) showed that the attack angle (β), longitudinal distance (X) and height (h) were the main parameters related to enhance heat transfer in the channel, so these three parameters were incorporated in the model.

Following the ribbed wall function methods proposed by Hanjalic and Launder (Hanjalic K. & Launder B.E., 1972), Donne and Meyer's wall (Donne M.D. & Meyer L., 1977), friction velocity in the channel with LVG could be modified as:

$$U'_{\mathrm{F}} = U_{\mathrm{F}}\left[\frac{1}{\kappa}\ln\left(\delta / h\right) + R\right] \tag{40}$$

where U'_{F} was modified friction velocity, and κ Karman constant, and R had an expression as:

$$R = 30\left(44^{\circ} / \beta\right)^{0.57}\left(X / \left(81h\right)\right)^{n}$$

where, $\mathrm{n} = -0.53\left(\beta / 90^{\circ}\right)^{-13}$ when $X / h < 81$; $n = 0.53\left(\beta / 90^{\circ}\right)^{-13}$ when $X / h \geq 81$.

Dimensionless temperature was modified as:

$$\left(t_{\mathrm{l}} - t_{\mathrm{w}}\right)\rho_{\mathrm{l}} c_{\mathrm{p}} U'_{\mathrm{F}}\left(h / X\right)^{0.5} / \left(15 q_{\mathrm{w}}\right) = Pr_{\mathrm{t}}\ln\left(\delta / h\right) / \kappa + \bar{G} \tag{41}$$

where $Pr_{\mathrm{t}} = 0.9$, and $\bar{\mathrm{G}}$ had an expression as:

$$\bar{G} = 8\left(h^{+} / 105\right)^{C1}\left(\beta / 44^{\circ}\right)^{C2}$$

where $h^{+} = h \cdot U'_{\mathrm{F}} / \nu$ ($C1 = 0$ when $h^{+} < 105$; $C1 = -0.03$ when $h^{+} \geq 105$; $C2 = 0.5$ when $\beta < 45^{\circ}$; $C2 = -0.45$ when $\beta \geq 45^{\circ}$.

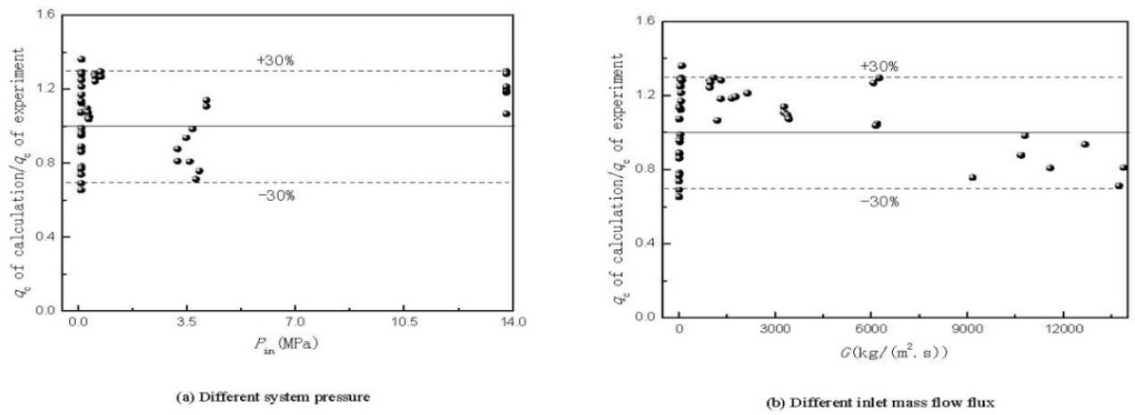

Figure 28. Comparison between calculation and experiment of CHF in the smooth channel.

The modified model was used to predict CHF in the channel with LVG, and the results were shown in Fig.29. It was seen that 93.7% of prediction data fell within ±30% of discrepancy band, the mean deviation was 3.6%, and the mean square root deviation of was 15.7%. In general, the modified model had a good accuracy, and it could be used to predict CHF in the channel with LVG.

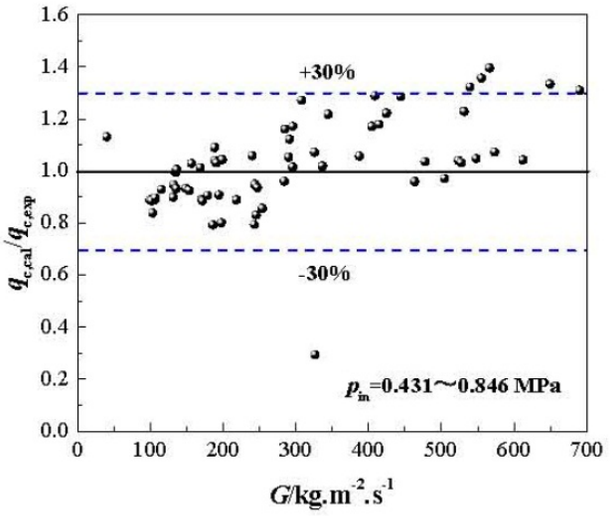

Figure 29. Comparison between calculation and experiment of CHF in the channel with LVG

7. Conclusions

In this chapter, aiming at thermal-hydraulical behavior in the smooth narrow rectangular channel and the LVGs machinednarrow rectangular channel, the systematical researches on the single-phase and two-phase Flow and heat transfer characteristics and their CHF behavior were carried out. The CFD method was used to optimize the configuration of the LVG machined narrow rectangular channel and to learn the Vortex behavior in LVGs channel and its effect on the flow and heat transfer characteristics with low pressure water being as working fluid in this project. In the single-phase flow state, the heat transfer capability in the LVG machined channel obviously increased with the friction pressure drop increase, but the effect of heat transfer enhancement is prominent. In the two-phase flow state, the boiling heat transfer coefficient increased also with the two-phase pressure drop increase. In the case of CHF, the CHF value in LVG machined channel was apparently improved with a quick two-phase pressure drop increase. But in the industrial application, the two-phase friction pressure drop in a equipment was not the majority of the whole system resistance, thus this heat transfer enhancement technology would have a bright future for industrial application. In this chapter, from the visualization experiments, the heat transfer enhancement mechanism of LV in the narrow rectangular channel was observed and analyzed and an analytical model for CHF in the narrow rectangular channel was represented and validated against the experimental data, the results could be used for similar researches.

Nomenclatures

A	area/m^2
a	single rib width/m
B	channel width/m
Bo	boiling number
b	single rib length/m
D	diameter/m

E	droplet entrainment fraction
f	friction factor
G	mass flow flux/kg·m^{-2}·s^{-1}
g	gravity acceleration/m·s^{-2}
H	channel height/m
h	Enthalpy/J·kg^{-1}; boiling heat transfer coefficient/W·m^{-2}·℃$^{-1}$; single rib height /m
j	dimensionless coefficient of heat transfer or superficial velocity/m·s^{-1}
L	length/m
m	droplet entrainment flow flux/kg·m^{-2}·s^{-1}
Nu	Nusselt number
Pr	Prandtl number
p	pressure/MPa
q	heat flux/W·m^{-2}
Re	Reynolds number
s	transverse distance in LVG configuration/m
T	temperature/℃
U , u	velocity/m·s^{-1}
W	mass flow rate/kg·s^{-1}
X	longitudinal distance in LVG configuration/m; Cartesian coordinate
Greek letters	
β	attack angle/°
δ	thickness/m
ϕ	effect factor
κ	Karman constant
λ	thermal conductivity/W·m^{-1}·℃$^{-1}$
μ	dynamic viscosity/kg·m^{-1}·s^{-1}
ν	kinematic viscosity/m^2·s^{-1}
ρ	density/kg·m^{-3}
σ	surface tension/N·m^{-1}
τ	shear stress/N·m^{-2}
Superscripts	
+	dimensionless symbol
Subscripts	
an	annular flow
av	average
c	critical
cal	calculation
d	droplet deposition
eb	broken bubble caused
ew	Vapor stream shear caused
exp	experiment
F	friction
g	gas phase

hy	hydraulic equivalent
in	inlet
l	liquid phase
lf	liquid film
lg	evaporation
m	mean
min	minimum
sub	subcooled
TP	two-phase
w	wall
∞	bulk flow

Author details

Yan-Ping Huang*, Jun Huang, Jian MA, Yan-Lin Wang and Jun-Feng Wang
CNNC Key Laboratory on Nuclear Reactor Thermal Hydraulics Technology, Chengdu, China

Qiu-Wang WANG
State Key Laboratory of Multiphase Flow in Power Engineering Xi'an Jiaotong University, Xi'an, China

Acknowledgement

This project is supported by the National Natural Science Fund (NO.50576089) in 2005, the Fund of Key Laboratory of Bubble Physics and Natural Circulation (NO.9140C7101030602) in 2006 and the National Natural Science Fund (NO.51176176) in 2012.

8. References

Chen, Q.Y., Zeng, M., Wang L., et al. (2006). Effect Longitudinal Vortex Generators on Convective Heat Transfer in Narrow Rectangular Channel, *J. Xi'an Jiaotong University*, vol. 40(9), pp. 1010-1013 (in Chinese).

Crecy F. (1994). The effect of grid assembly mixing vanes on critical heat flux values and azimuthal location in fuel assemblies, *Nuclear Engineering and Design*, Vol. 149, pp. 233-249.

Donne M.D. & Meyer L. (1977). Turbulent convective heat transfer from rough surfaces with two-dimensional rectangular ribs. *Int. J. Heat and Mass Transfer*, 20: 583-620.

Fedorov A.G. & Viskanta R. (2000). Three-Dimensional Conjugate Heat Transfer in the Microchannel Heat Sink for Electronic Packaging, *Int. J. Heat and Mass Transfer*, Vol. 43(3), pp. 399-415.

Gungor KE, Winterton RHS. Simplified General Correlation for Saturated Flow Boiling and Comparisons of Correlations with Datas[J]. Chem Eng Res Des, 1987, 365: 148-165.

* Corresponding Author

Hanjalic K. & Launder B.E. (1972). Fully developed asymmetric flow in a plane channel. *J. Fluid Mech*. 51, Part 2: 301-335.

Islam, M.S., Hino, R., Haga, K., et al. (1998). Experimental Study on Heat Transfer Augmentation for High Heat Flux Removal, *J. NUCLEAR SCIENCE and TECHNOLOGY*, vol. 35(9), pp. 671-678.

Jackey, H.S., Roarty, J.D. and Zerbe, J. E.(1958). Investigation of Burnout Heat Flux in Rectangular Channels at 2000 Psia, Trans. ASME, vol. 80, 391.

Johnson T.R. & Joubert P.N. (1969). The Influence of Vortex Generators on Drag and Heat Transfer from a Circular Cylinder Normal to an Airstream, *Heat Transfer*, Vol. 91, pp. 91-99.

Joel, W. (1992). The current status of theoretically based approaches to the prediction of the critical heat flux in flow boiling, Nuclear Technology, vol. 99, pp. 1-21.

Kays, W.M. & Clark. S.H. (1953). TR no.17, Department of Mechanical Engineering, Stanford University, Stanford ,California, August 15.

Kafengauz, N. L. and Bocharov, I. D. (1959). Effect of Heat Transfer for Water by Gap Width of Narrow Rectangular Channel, Teplocncrgetika, vol. 3, pp. 76-78.

Kaotaoka, I., Ishii, M., Mishima, K. (1983). Genertation and size distribution of droplet in gas-liquid annular two-phase flow, ASME J Fluids Engineering, vol. 105, pp. 230-238.

Ma J. (2008). Investigation on heat transfer enhancement of longitudinal vortices in narrow rectangular channel with single-phase water, Nuclear Power Institute of China (in Chinese).

Mishima, K., Ishii, M. (1984). Flow Regime Transition Criteria for Upward Two-phase Flow in Vertical Tubes, Int. J. Heat and Mass Transfer, vol. 27(5), pp. 723-737.

Metha R.D. & Bradshaw P. (1988). Longitudinal vortices imbedded in turbulent boundary layers, Part 2. Vortex Pair with 'Common Flow' Upwards, *J. Fluid. Mech*., Vol. 188, pp. 529-546.

Schubauer, G.B. & Spangenberg. (1960). WG. Forced Mixing in Boundary Layers, *Fluid Mech*, Vol. 8, pp. 10-31.

Shah, R.K. & A.L. (1978). London: Laminar Flow Forced Convention in Ducts, *Advances in Heat Transfer*, Academic Press, New York.

Sohankar, A. & Davidson, L. (2001). Effect of inclined vortex generators on heat transfer enhancement in a three-dimensional channel, *Numerical Heat Transfer, Part A: Applications*, vol. 39, no. 5, pp. 433-448.

Veda, T., Inoue, M., Nagatome, S. (1981). Critical heat flux and droplet entrainment rate in boiling of falling liquid films, Int. J. Heat and Mass Transfer, vol. 24(7), pp. 1257-1266.

Wang, L., Chen, Q.Y., Zhou, Y.G. (2005). Heat Transfer Enhancement in Rectangular Narrow Channel with Periodically Mounted Longitudinal Vortex Generators on One Sidewall, *Nuclear Power Engineering*, vol. 26(4), pp. 344-347 (in Chinese).

Wang, Q.W., Chen, Q.Y., Wang, L., et al. (2007). Experimental study of heat transfer enhancement in narrow rectangular channel with longitudinal vortex generators, *Nuclear Engineering and Design*, vol. 237, pp. 686–693.

Yun JY, Lee KS. (2000). Influence of design parameters on the heat transfer and flow friction characteristics of the heat exchanger with slit fins. *International Journal of Heat and Mass Transfer*, 43: 2529-2539.